IEEE Access
Multidisciplinary | Rapid Review | Open Access Journal

Date of publication xxxx 00, 0000, date of current version xxxx 00, 0000.

Digital Object Identifier 10.1109/ACCESS.2022.Doi Number

Modelling of Inductances Considering Bar Harmonics and Temperature to Accurately Predict Output Torque of an Induction Motor

Areej Fatima[1] (Student Member, IEEE), Rajendra Kumar[1] (Member, IEEE), Ze Li[1] (Member, IEEE), Glenn Byczynski[2] (Member, IEEE), and Narayan C. Kar[1] (Senior Member, IEEE)

[1]University of Windsor, ON N9B 3P4, Canada
[2]Nemak USA/CAN, Windsor, ON N9C 2L1, Canada

Corresponding author: Areej Fatima (fatim119@uwindsor.ca)

This work was supported by the Canada Research Chair Program (Ref. no. CRC-2019-00319), NSERC, Ford Motor Company of Canada, Nemak Engineering Centre for funding support to this work.

ABSTRACT Equivalent circuit parameters of an induction motor are highly susceptible to various undesired factors. These phenomena primarily include effects of higher order time and space harmonics, temperature, magnetic saturation, and skin-effect. Traditional approaches model these equivalent circuit parameters via temperature, iron saturation, and slotting effects. However, the impacts of harmonic fields generated by the spatial magnetomotive force components as well as that of skin effect in motor inductances are not considered. The proposed work therefore presents an improved inductance estimation considering the impact of total harmonic distortion in the magnetomotive force with a power function–based formulation. Since the induction motor performance is sensitive to its rotor circuit parameters, another realistic variation taken up in this work includes the impact of iron saturation, and skin effect altogether on rotor leakage inductance and rotor bar resistance. Additionally, the effects of non-linearity, such as temperature variations, are incorporated into the magnetizing inductance, while the permeance of rotor tooth-bridge segments is considered in the rotor leakage inductance and bar resistance. The effectiveness of the proposed model is demonstrated with simulation and experimental results of a 13 kW three–phase induction motor prototype for a wide range of operations. This method significantly improves the modelling of inductances, enhancing the accuracy of the electromagnetic torque predictions over a wide range of operating speeds. Achieving net-zero carbon emissions is crucial for transportation electrification, which necessitates the use of high-speed traction motors in electric vehicles that require a reliable design. Therefore, an improved method is proposed that effectively captures the non–linear effects in predicting the parameters and performance including the output torque of the machine.

INDEX TERMS Electromagnetic torque, harmonic distortion, induction motor, leakage saturation, skin effect, temperature effect.

I. INTRODUCTION

Electric vehicles (EVs) are exponentially capturing the attention of the automotive companies owing to their significant contribution to net zero carbon emissions [1]. To satisfy the growing demand for EVs, researchers are striving to meet the requirements of automotive manufacturers such as cost–effective, high–power electric motors tailored for transportation electrification applications [2], [3]. Thus, induction motors (IMs) are regaining popularity in the industry due to the elimination of permanent magnets from the rotor assembly, their rugged structure, and reduced susceptibility to supply chain issues [4]. The capability of IMs to be operated in saturation mode under normal conditions reinforces their ability to withstand elevated temperatures which enhances their usage in the transportation sector, thereby promoting their increased utilization [5].

High accuracy of parameter determination is important to ensure the dynamic operation of the traction IM in an EV. For traction applications, the target for IMs is to attain high performance with improvement in efficiency by reducing the core loss and copper loss [6] resulting in reduced surface

temperature. For IM design, there is a trade–off between the surface temperature and the volume of the motor to deliver high torque while targeting increased torque density. In order to deliver high output torque under a fixed volume, IMs draw more magnetizing current to compensate for the required output torque, affecting the power factor of the motor [7], [8]. Due to the high magnetization current, the magnetic saturation in the core is increased, thus affecting the efficiency. Several researchers are aiming toward reducing core saturation, given volume as a constraint, thus, on the design level, contemplating the effects of saturation is important [9], [10]. Moreover, various slotting parameters, particularly with semi–closed slots, have a significant impact on saturation. Due to the varying reluctance in the air gap affecting the air gap flux density and resulting in the occurrence of spatial harmonics. Additionally, at higher frequencies, the rotor bars induce a higher amount of eddy current concentrated towards the outer surface of the conductor [11]–[14]. Furthermore, non-uniformities in the rotor flux distribution caused by rotor MMF lead to the production of rotor bar harmonics, which affect the performance of the motor [15]. The rotor bar harmonics induce a skin effect resulting in high–frequency eddy current that flows towards the outer surface of the conductor, making the impact significant. Therefore, the performance prediction of IMs requires additional information of the non–linearities to determine the traction motor electrical parameters such as resistances and inductances, and performance characteristics such as total core loss, and electromagnetic torque accurately.

In the existing literature [5], [16]–[19], the deep bar effect is taken into account, however, motor performance, particularly torque, is impacted by neglecting the bar harmonics resulting from the skin effect. In [20], [21], the skin effect due to deep rotor bars is considered since the effective rotor inductance and rotor resistance are varied as a function of rotor frequency. Conversely, the effect of rotor bar harmonics, the skin effect induced due to bar harmonics, and temperature effect are not considered in the methodology, influencing the prediction of torque as well. In [22], [23], non–linear inductance is modelled using power functions. However, the mutual saturation is neglected, along with the skin effect and rotor bar harmonics. According to [24], the methodology using the power functions considered the mutual saturation effect on magnetizing and rotor leakage inductance. Since the impact of the mutual saturation is considered on the rotor leakage, the skin effect induced due to the bar harmonics affecting the bar leakage flux is not modelled in [24].

The impact of rotor MMF harmonics on motor performance considering the flux density, eddy currents, and torque is investigated in [25]. However, the effect of deep rotor bars is neglected in terms of skin effect, and the induced skin effect due to the bar harmonics. The significant effect on magnetizing and rotor leakage inductances is ignored. Furthermore, as referenced in [26], [27], saturation occurs due to the induction of high–frequency eddy current in the bars, and hence the bar leakage inductance changes with the bar current. Therefore, the methodology carried out in [26], [27] analyzes the air gap field harmonics and time harmonics in stator windings due to the closed rotor bar's bridge saturation ignoring the slot harmonics, and skin effect due to the deep bar harmonics.

Furthermore, in comparison with shallow rotor bars, deep rotor bars have higher reactance and leakage flux in the core [13], [14], [28]. As reported in [14], electrical parameters including resistance and reactance of equivalent circuit are determined considering the skin effect in the rotor bars by implementing the multilayer approach. However, the major setback is that the effect of leakage flux is not considered while formulating the skin effect, while skin effect increases the leakage flux. Skin effect in the rotor bars causes bar harmonics that redistribute the magnetic field in the rotor core encircling the rotor bars. The generated bar harmonics significantly impact the magnetizing and rotor leakage inductance of the traction motor. The harmonics with higher amplitude lead towards saturation in the core, reducing the material permeability and inductance, which is ignored. Moreover, in [29] rotor bar currents are determined, however, the effect on the iron core loss and the skin effect induced due to the rotor bar currents are not considered in the modelling. Thus, affecting the prediction of the steady–state performance of the IM which needs to be taken into account for traction application such as electromagnetic torque.

Observing the above–mentioned shortcomings of the traditional models, the objective of the work presented in this manuscript is to:

1) Analyze and incorporate the impact of MMF harmonics on the motor inductances with a proposed univariable power function–based formulation.
2) Investigate and consider the effect of temperature on magnetizing inductance using a proposed univariable power function–based formulation.
3) Put forward a comprehensive formulation to account the impact of enhanced rotor tooth–bridge segments' permeance for accurate estimation of rotor leakage inductance and rotor–bar resistance.

While proposing the modelling for the above–mentioned shortcomings, the impacts of magnetic saturation, cross saturation, and skin effects are carried forwarded from the available literature [20], [24], to improve the electromagnetic torque prediction of IM.

The paper is organized as follows: Inductance modelling considers the effects of MMF harmonics using a power function, as detailed in Section II, and adjustments are made to add the effect of the temperature in the resistance and magnetizing inductance formulations. Section III determines the power–based formulations' variables using regression analysis by considering motor losses. Section IV thoroughly compares the experimental, FEA–based, proposed method, and conventional method to draw a comparison based on the accuracy of the performance prediction by making the

formulations of electrical parameters accurate. The conclusions are drawn in Section V.

II. INDUCTANCE MODELS WITH CONSIDERATION OF MMF HARMONICS

Among the five parameters of a conventional T-equivalent circuit of an IM, direct measurement is only available for the stator winding resistance whereas all other four parameters are determined with the effect–based observations. All these four parameters are highly susceptible to field distribution diverged by the MMF harmonics and cross couplings along with the magnetic non–linearity. The impact of magnetic non–linearity and cross coupling is widely discussed in the literature [20], [24], whereas the harmonic distortion in MMF distribution is not covered in the literature. Therefore, this section presents the models for magnetizing inductance, rotor bar leakage inductance and rotor resistance with the consequences of the MMF harmonics. Figure 1 shows the FEA–based semi–closed 13 kW squirrel cage induction machine (SCIM), and Table I explains the geometrical parameters labelled in Fig. 1.

A. PROPOSED TOTAL HARMONIC ORDER–BASED POWER FUNCTION FOR MAGNETIZING INDUCTANCE

MMF harmonics produce non–uniformities in the distribution of flux in the rotor core, affecting the magnetizing inductance since the flux density is varied. This leads to a significant variation in the motors' permeability affecting the magnetizing inductance. With the higher amplitude of harmonic contents in the MMF in several core regions of the motor, the corresponding regions will be saturated therefore the magnetizing inductance will be affected. Furthermore, any change in rotor resistance due to temperature and skin effect increases the magnetizing inductance. At higher loads, temperature tends to elevate thus resistance also increases, limiting the flow of the rotor current under a fixed voltage. This leads to an overall change in the impedance of IM design.

The conventional expression for the magnetizing inductance of a three–phase IM with saturation of iron is given by (1),

$$L_m(\varphi_s,\varphi_\sigma)=\left(\frac{\sigma_{Al}\mu_0(T_{ph}K_w)^2}{\pi^2}\right)\left(\frac{L\tau'}{pgK_cK_{sat}(\varphi_s,\varphi_\sigma)}\right) \quad (1)$$

where, σ_{Al}, and μ_0 represents the conductivity of aluminum, and permeability of free space, respectively. Moreover, T_{ph}, K_w, L, τ', p, g, K_c, L_m denotes turns per phase, winding factor, stack length, pole span, pole pairs, air gap length, Carter's coefficient, and magnetizing inductance, respectively. φ_s, and φ_σ appear as stator flux and rotor leakage flux, correspondingly. The saturation factor K_{sat} is reported with the saturation due to the main stator flux and cross-saturation as

$$K_{sat}(\varphi_s,\varphi_\sigma)=1+\alpha\varphi_s^a+\frac{\gamma L_m'}{d+2}\varphi_s^c\varphi_\sigma^{d+2} \quad (2)$$

where, $(\alpha, \gamma, u, \tau) \geq 0$ and $(a, d, c, m) \geq 0$. The value of K_{sat} in (2) in fact depends upon the power supply fed to the motor.

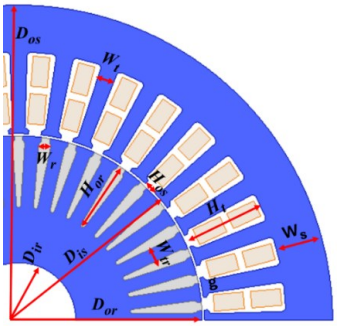

FIGURE 1. FEA-based semi-closed 13 kW traction IM.

TABLE I
GEOMETRIC DIMENSIONS OF 13 KW TRACTION IM

Parameter	Definition	Values (mm)
D_{os}	Stator outer diameter	152.062
D_{is}	Stator inner diameter	90.062
W_t	Stator tooth width	3.12
W_s	Stator yoke width	11.31
H_t	Stator slot depth	19.62
H_{os}	Stator slot opening	3
W_r	Rotor bar width	2.885
H_{or}	Rotor bar depth	16.72
W_{tr}	Rotor tooth width	3.46
g	Air gap length	0.581
D_{or}	Rotor outer diameter	88.9
D_{ir}	Rotor inner diameter	27.668

For a specific motor geometry, (1) can be expressed with power supply dependent variables as

$$L_m(\varphi_s,\varphi_\sigma)=K\left(\frac{A_p}{K_{sat}(\varphi_s,\varphi_\sigma)}\right) \quad (3)$$

where, K represents the constant and A_p determines the area. The conventional expressions of [20], [24], cover only the impact of saturation and cross saturation while using (3). However, with the presence of rotor bar harmonics, the skin effect produced by these harmonics results in the decrement of the overall cross–sectional area available for main flux. Therefore, considering the impact of total harmonic distortion (THD), the two–variable expression for L_m becomes a three–variable expression by making the area under pole a univariable function of THD as

$$A_p \rightarrow A_p(\tau) \Rightarrow L_m(\varphi_s,\varphi_\sigma,\tau)=\frac{L_m}{A_p}\frac{A_p(\tau)}{K_{sat}(\varphi_s,\varphi_\sigma)} \quad (4)$$

$$\tau=\frac{\sqrt{\sum_{n=2}^{\infty}F_r^2}}{F_{r1}} \quad (5)$$

where, τ denotes THD of bar harmonics F_r, and n represents the harmonic order. Since, the impact is monotonic with the increasing quotient of harmonics in the fundamental flux, its incorporation in a simpler form can be modelled as

$$A_p(\tau)=\frac{A_p}{1+u\tau^m} \quad (6)$$

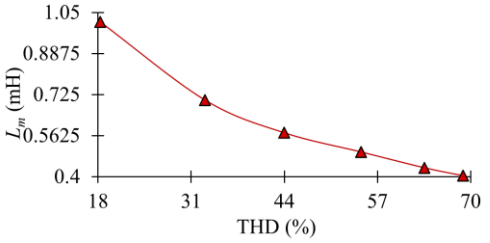

FIGURE 2. Impact of bar harmonics THD on magnetizing inductance at the rated speed 3,000 rpm.

The significant impact of bar harmonics THD on magnetizing inductance is shown in Fig. 2. The conventional equations are improved [24]. Therefore, the magnetizing current becomes as

$$I_{m\_\tau}(\varphi_s,\varphi_\sigma)=\frac{\varphi_s}{L_m}\left[\left(1+\alpha{\varphi_s}^{a}+\frac{\gamma L_m}{d+2}{\varphi_s}^{c}{\varphi_\sigma}^{d+2}\right)\left(1+u\tau^m\right)\right] \quad (7)$$

where, I_{m_τ} presents as magnetizing current. The inductance corresponding to (7) is follows

$$L_{m\_\tau}(\varphi_s,\varphi_\sigma)=\frac{L_m}{\left(1+\alpha{\varphi_s}^{a}+\frac{\gamma L_m}{d+2}{\varphi_s}^{c}{\varphi_\sigma}^{d+2}\right)\left(1+u\tau^m\right)} \quad (8)$$

B. CALCULATION OF STATOR RESISTANCE CONSIDERING THE TEMPERATURE EFFECT

Non–linear effects such as temperature effect is considered to determine the effective resistance R_{eff}. The raw value of stator resistance without considering the temperature effect denoted as R_s is updated using a skin effect factor K_{skin}. Resistance varies with the rising temperature and for IMs to attain higher accuracy in the performance prediction, temperature effect is taken into account.

$$R_{eff}=R_sK_{skin}=\left(R_s+\Delta R\right)K_{skin} \quad (9)$$

$$\Delta R=R_s\alpha\times\Delta T\Rightarrow R_{eff}(T)=R_s\left(1+\alpha\times\Delta T\right)K_{s\_skin} \quad (10)$$

where, ΔR determines the change in temperature, ΔT is the difference between the final and the reference temperature, and α represents the temperature coefficient that varies with the temperature. The motor under test (MUT) uses a double layer winding, therefore, skin effect in stator winding is considered with p^{th} layers. ξ is a dimensionless parameter representing the ratio of skin depth to the radial distance from the center of the conductor [30].

$$K_{skin}=\left(\xi\frac{\sinh(2\xi)+\sin(2\xi)}{\cosh(2\xi)-\cos(2\xi)}\right)+\left(p^2-p\right)\left(2\xi\frac{\sinh(\xi)-\sin(\xi)}{\cosh(\xi)+\cos(\xi)}\right) \quad (11)$$

where,

$$\xi=\left(\sqrt{\frac{s\omega\mu_0\sigma_{Al}zH_o}{2H_w}}\right)\times h \quad (12)$$

where, ξ denotes the ratio between the height of the stator conductor and the depth of field penetration in the stator conductor at a particular frequency ω. Furthermore, z represents the conductor in series in a slot, H_w denotes the width of the stator slot, and H_o depicts the width of the stator conductor. The skin effect is affected due to the magnetic saturation in the core. Saturation varies the magnetic permeability of the surrounding medium altering the penetration depth of the skin effect. To consider the effect of saturation in total resistance, (10) is equated with (13) to attain (15). Using (15), skin and temperature effects vary the permeability to obtain the effective permeability. Moreover, using the effective permeability the total resistance is determined for the stator windings.

$$R_{eff}=R_s\times\frac{\delta_{eff}}{\delta_{DC}}=R_s\times\sqrt{\frac{\mu_r}{\mu_{eff}}} \quad (13)$$

$$\mu_{eff}=\frac{\mu_r}{\left((1+\alpha\times\Delta T)K_{s\_skin}\right)^2} \quad (14)$$

$$R_{total}(T)=R_{eff}(T)R_{eff}=R_s^2(1+\alpha\times\Delta T)K_{s\_skin}\times\sqrt{\frac{\mu_r}{\mu_{eff}}} \quad (15)$$

where, δ_{eff}, and δ_{dc} represents the effective skin depth of the stator conductor under the AC supply, and DC skin depth. However, these terms are converted to the relative and effective permeability considering the impact of skin and temperature. Thus, the final equation proposes the effect of the temperature, skin, and saturation by interlinking each non–linearity.

C. CALCULATION OF MAGNETIZING INDUCTANCE CONSIDERING TEMPERATURE IMPACT

Magnetizing inductance is primarily related to the motor windings generating the magnetic field which interacts with the rotor to produce flux in the core. Therefore, magnetizing inductance indirectly affects the majority of the flux that flows in the core. Since rising temperature influences the relative permeability of the core material, the impact of the elevated temperature is reproduced on the magnetizing inductance. Using the univariable power function–based formulation, the temperature impact is considered in the magnetizing inductance. Equations (7), and (8), are modified to (16), and (17) by adding the temperature effect as it shares the direct relation with the magnetizing inductance for the temperature the prototype is tested for. The conventional equations are improved [24].

$$I_{m\_\tau}(\varphi_s,\varphi_\sigma)=\frac{\frac{\varphi_s}{L_m}\left[\left(1+\alpha{\varphi_s}^{a}+\frac{\gamma L_m}{d+2}{\varphi_s}^{c}{\varphi_\sigma}^{d+2}\right)\left(1+u\tau^m\right)\right]}{\beta^{(T\times e)}} \quad (16)$$

$$L_{m\_\tau}(\varphi_s,\varphi_\sigma)=\frac{L_m\times\beta^{(T\times e)}}{\left(1+\alpha{\varphi_s}^{a}+\frac{\gamma L_m}{d+2}{\varphi_s}^{c}{\varphi_\sigma}^{d+2}\right)\left(1+u\tau^m\right)} \quad (17)$$

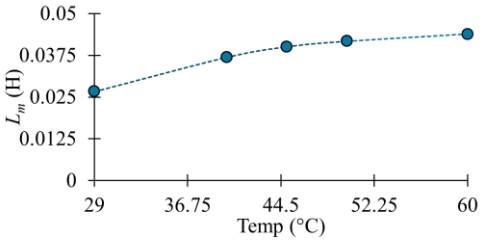

FIGURE 3. **Variation in magnetizing inductance at an increasing temperature at the rated speed 3,000 rpm.**

where, $\beta \geq 0$, and $(e) \geq 0$. It is shown in Fig. 3, that at the rated speed of 3,000 rpm, at various temperatures the behavior of magnetizing inductance is observed using the laboratory prototyped 13 kW IM.

D. IMPROVED CALCULATION OF ROTOR CIRCUIT PARAMETERS WITH MMF HARMONICS

In this section, the electrical parameters are modified by incorporating the effect of the slot leakage flux in determining the rotor leakage inductance. Incorporating this impact with the skin effect in the rotor bars improves the accuracy in determining the bar resistance, and rotor leakage inductance.

1) INCORPORATING THE EFFECT OF TOOTH–BRIDGE SEGMENTS PERMEANCE IN ROTOR BAR RESISTANCE

For the rotor bar structure, the skin effect varies significantly from the rotor slot opening to the bottom of the rotor slot. The skin effect increases the effective resistance of the rotor bars since the current is concentrated around the opening of the bar [28]. The non–uniform current distribution influences the distribution of the magnetic flux making it uneven within the rotor core. This results in localized saturation in some regions of the core potentially increasing the reluctance in the saturated regions. Due to the localized saturation in the core, the effective permeability of the material is reduced eventually increasing the reluctance. Furthermore, the localized saturation is one of the main sources of distorting magnetic field lines leading towards non–uniform flux density. Additionally, the core losses are increased, elevating the temperature of the machine, and degrading the efficiency. Therefore, a novel methodology considering the effect of the permeance of rotor tooth–bridge segment in the rotor bar resistance formulation is developed, which is ignored in the traditional methodology [20], [24]. The proposed method formulates the skin effect as a function of leakage flux that could potentially lead towards saturation. To consider the slot leakage flux in the skin effect on the rotor bar, as shown in Fig. 4, the closed loop of slot leakage flux is considered for each layer. Since each layer leakage flux contributes to the saturation of the core.

$$L_{eff} = \frac{W_t}{\mu_0} + \oint_L \frac{dL}{\mu_{r\_core}(B_r)} \tag{18}$$

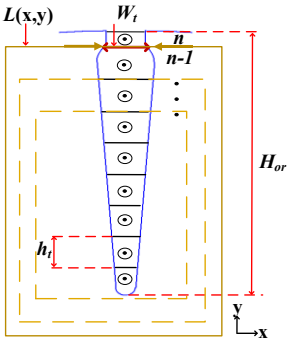

FIGURE 4. **Skin effect of rotor bar considering the closed loop of the leakage flux.**

$$\frac{L(x,y)}{\mu_{eq}(B_r)} = \frac{W_t}{\mu_0} + \frac{L(x,y)}{\mu_{core}(B_r)} \tag{19}$$

$$\Delta\varphi_p = \left(\frac{\mu_0}{L_{eff}}\right) l_{stack} h_t \sum_{j=1}^{p} I_j \tag{20}$$

where, L_{eff}, φ_p, and I_j shows the effective length of the slot leakage flux, flux linkage, and current in each layer of rotor bars. Distribution of flux density is used to evaluate (18) – (20) corresponding to the variation of permeability. Section III details the procedure followed in this work to get the flux density distribution. Following (20), the closed loop of slot leakage flux L for each layer is used to determine its impact on rotor bar resistance variation as (21).

$$R_p = \left(\frac{l_{stack}}{h_t} \sum_{j=1}^{p} I_j\right)\left(\frac{\mu_0}{W_t} + \frac{\mu_{core}(B_r)}{L(x,y)}\right) \tag{21}$$

where R_p determines the rotor bar resistance considering the effect of the slot leakage flux in the induced skin effect to attain higher accuracy.

2) ROTOR BAR INDUCTANCE CONSIDERING THE IMPACT OF TOOTH–BRIDGE SEGMENTS' PERMEANCE

In this section, unlike the existing method [20], [24], the rotor leakage inductance is modified to incorporate the impact of the leakage flux of rotor bars in the rotor core. The conventional rotor leakage inductance is modified to incorporate the impact of enhanced rotor tooth–bridge segments' permeance for determining rotor leakage inductance [30]. The skin effect phenomena induce a non–uniform high frequency eddy current in rotor bars directed towards the outer surface. Due to the non–uniform current density, the magnetic field density generated in the rotor core is altered henceforth affecting the rotor leakage flux. Thus, the variation in the field strength across rotor surface cross–sectional area leads toward the un–even distribution of the leakage flux. Moreover, skin effect mainly occurs due to the interaction of the time varying magnetic field and the conductivity of the bar which results in the displacement of the current towards the rotor bar's periphery. Using (20), the effect of skin effect is considered on

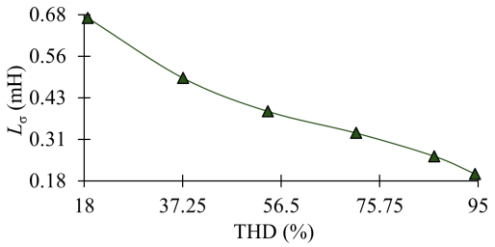

FIGURE 5. Impact of bar harmonics THD on rotor leakage inductance at 3,000 rpm using blocked rotor test.

rotor leakage inductance. The significant impact of bar harmonics THD on the rotor leakage inductance is shown in Fig. 5.

$$L_p = \left(\frac{\mu_0}{L_{eff}}\right) l_{stack} h_t \tag{22}$$

$$L_{\sigma\_\tau}(\varphi_s, \varphi_\sigma) = \frac{L_\sigma}{\left(1+\beta\varphi_\sigma{}^{b} + \frac{\gamma L_\sigma}{c+2}\varphi_s{}^{c+2}\varphi_\sigma{}^{d}\right)\times(1+u\tau^m)L_p} \tag{23}$$

where, L_p determines the rotor inductance derived using (20) to attain the final value of the rotor leakage inductance using (23).

III. REGRESSION ANALYSIS WITH ADDITIONAL LOSSES

Based on the proposed method, an equivalent circuit model is modified in terms of electrical parameters such as resistances, and inductances, as shown in Fig. 6. Correction for the eddy currents impact on magnetizing current and consequently on the values of the magnetizing inductance is considered by calculating the core loss as per [31], [32].

$$P_{core} = K_h f B^{\Gamma} + K_{skin} K_e f^2 B^2 + K_{ex} f^{1.5} B^{1.5} \tag{24}$$

The determined inductances using (17), and (23) correspond to the magnetic flux linkage due to the stator current in the winding. During the operation of MUT under steady–state condition, the core losses contribute to the impedance that encounters the voltage drop due to the core loss resistance in the circuit. This affects the voltage and current relationship by contributing to the voltage drop. The laboratory IM uses steel M19–29G as a core material, and Fig. 7 shows the family of curves over a wide range of frequency and flux density.

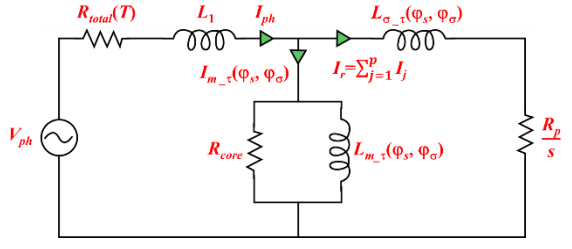

FIGURE 6. Improved equivalent circuit model using improved power–based inductances modelling and resistances considering machine non–linearities.

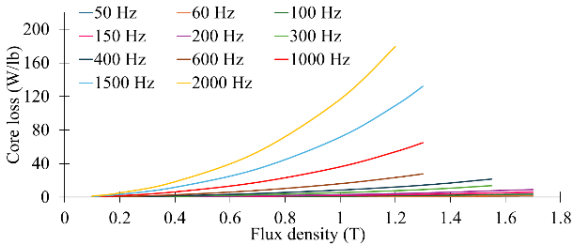

FIGURE 7. Family of curves for AK steel M19–29G over a wide range of frequency.

A. INTER–BAR CURRENT IN THE ROTOR

Inter–bar current predominantly contributes to the rotor copper loss. The active loss created by the excess active power loss with these inter bar currents is added in the rotor copper loss to precisely determine the rotor leakage inductance values [30], [33]. Due to the uninsulated rotor bars, the additional inter–bar current occurs between the consecutive rotor bars, through the rotor core. Furthermore, the impact of the cross–path is determined using a resistance value and this resistance is significantly larger than the iron core loss resistance. Moreover, the rotor lamination is divided into several segments, and each segment defines the inter–bar current lumped resistance. According to [30], the mathematical relationship is formulated between the consecutive rotor bars and the cross–path resistive currents as

$$I_{\text{int\_bar}} = j\frac{e^{-\left(j\pi v/N_r\right)}}{2\sin\frac{\pi v}{N_r}}\left(I_{bar}\right)_{k=l_{stack}/2} \tag{25}$$

where, I_{int_bar}, v, N_r, and I_{bar} depicts the inter–bar current, harmonic order, number of rotor bars, and the rotor bar current.

B. PARAMETER IDENTIFICATION

Parameters including {u, β,}, and {m, e} are extracted based on non–linear regression method. Using the proposed equations considering the above–mentioned parameters, a mathematical model that expects a relationship between the variables is established. Furthermore, after the identification of the parameters as shown in Table. II, the selected model is fitted to the data by using the identified parameters into the

TABLE II
FITTED PARAMETERS BASED ON NON-LINEAR REGRESSION

Magnetizing Inductance	
Parameter	**Value**
u	-0.9977
m	0.0004564
β	0.00343
e	0.6324
Rotor Leakage Inductance	
Parameter	**Value**
u	-0.07811
m	0.5095

chosen model equations. For the parameters {α, γ}, and {*a*, *d*, *c*} the values are considered from [24]. The evaluation flow using the power function–based inductances modelling incorporating non–linearities is represented in Fig. 8.

IV. EXPERIMENTAL VALIDATION OF MAGNETIZING INDUCTANCE AND TORQUE USING 13 kW IM

The electromagnetic performance characteristics such as output torque at various frequencies is experimentally validated. For experimental verification, a laboratory–prototyped 13 kW IM as shown in Fig. 9 is used. The electrical and material specifications are enlisted in Table III. The dynamometer is coupled with the MUT and a variable frequency device (VFD) with an integrated inverter is connected with the MUT. Two gear ratios are developed to operate the MUT at high speed (3.47:1), and high torque (1:1) considering the limitation on the dynamometer. Using VFD, at various DC voltage levels, no–load and on–load testing is conducted for a wide range of frequencies and loading levels. For experimentation, using VFD at a standstill condition, the electrical parameters including stator resistance, and stator inductance are attained. Furthermore, using the proposed method, the identified electrical parameters are accurately predicted including the output torque using (26), and magnetizing inductance, to draw a comparison with the experimentally validated data. The experimental data is taken at the same temperature of 40 degrees Celsius at varying operating conditions.

$$T_e = \frac{3V_{ph}^2(R_p/s)}{\omega_s(R_{total}(T)+R_p/s)^2+(2\pi f(L_1+L_{\sigma\_\tau}))^2} \quad (26)$$

where, V_{ph} represents the phase voltage, and s denotes the slip.

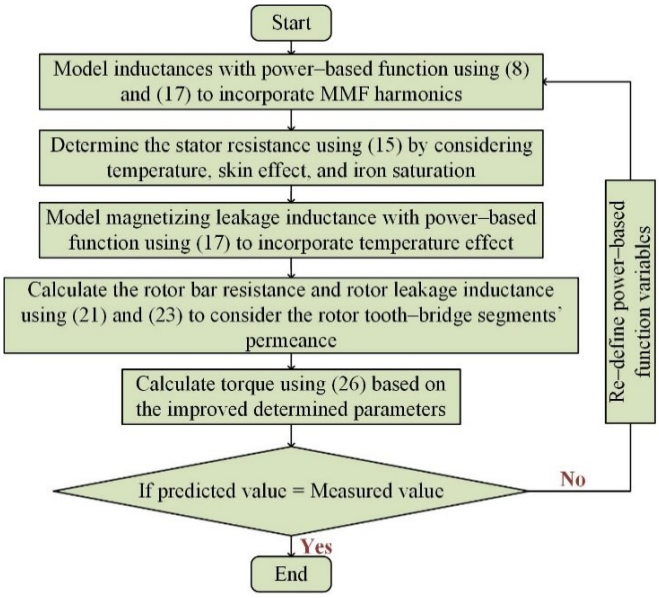

FIGURE 8. Flowchart representation of the proposed methodology.

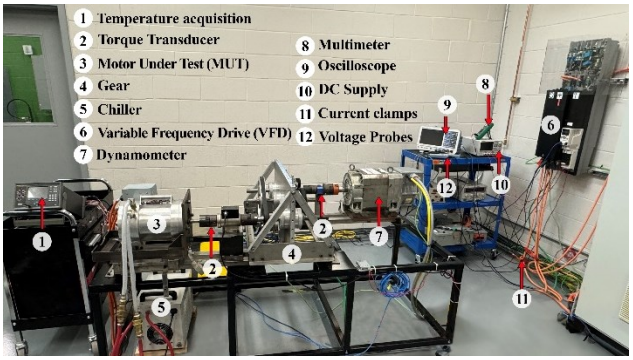

FIGURE 9. Experimental test setup of laboratory prototyped traction IM.

TABLE III
ELECTRICAL PARAMETERS OF TESTED MUT

Parameter	Value
Synchronous speed (rpm)	3,000
Electrical steel	M19–29G
Rated power (kW)	13
Rated AC voltage	285
Rated current (A)	30
Stator resistance (Ω)	0.2185
Rated frequency (Hz)	100

A. RELATION OF VOLTAGE AND CURRENT UNDER FIXED TORQUE

The relation of stator input current is investigated with the varying level of voltage under a given torque. Under a fixed demand of torque, increasing voltage allows MUT to draw more stator current in order to meet the demand of torque. As torque is directly proportional to magnetic field strength, higher voltage creates a stronger magnetic field that requires more stator current to maintain the torque. A comparison of FEA simulated, and experimentally measured data is made with the proposed and conventional method to compare with the existing state–of–art. A comparison is drawn in Fig. 10 (a), (b), and (c) illustrating the above–mentioned behavior of the motor under three sets of different torques to show the behavior over the wide range.

As shown in Fig. 10(a), a comparison is drawn for a fixed torque of 15 Nm in the MTPA region where a gear ratio (1:1) is used. Using the proposed methodology, the prediction is improved by 5.31% when compared with the experimentally measured data as compared to the conventional method predicting the performance with an accuracy of 8.83%.

Furthermore, as shown in Fig. 10(b), using the proposed method the prediction is improved by 5.53% as compared to the conventional method showing 11.20% considering the measured data as a reference. The last two points are taken from the flux weakening (FW) region, therefore current is lower in that region as compared to the MTPA region. Finally, Fig. 10(c) determines an improvement in accuracy by 5.60% using the proposed method, however, the conventional method shows an accuracy of 11.40%, when compared to the measured data, respectively.

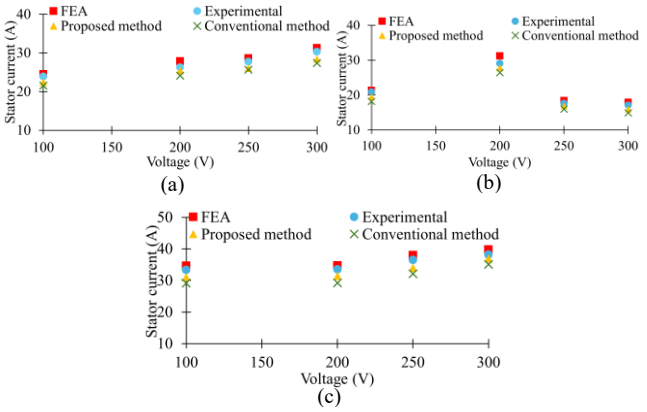

FIGURE 10. Profile of input stator current at various voltage levels under fixed torques. (a) Under MTPA region at 15 Nm. (b) Under MTPA and FW region (last two data points) at 8Nm. (c) Under MTPA region at 25 Nm.

B. RELATION OF CURRENT AND SPEED AT A VARYING TORQUE AND FIXED VOLTAGE LEVEL

In this section, the relation of the stator input current is investigated with respect to the rotor speed (rpm) under a fixed voltage level. The rotor speed is controlled by slip frequency, thus when rotor speed increases indicating a decrement in the slip, the induced rotor currents increase. Due to the increase in the rotor current, the impedance is affected and therefore more input stator current is drawn to maintain the demand torque. It can be seen in Fig. 11(a), under a fixed voltage of 100 V in the MTPA region, the accuracy of the proposed method is improved by 4.53%, whilst the accuracy of the conventional method is approximately 10.60%, considering the measured data as a reference.

Furthermore, Fig. 11(b) illustrates the comparison for 200 V, the average discrepancy of stator current prediction using the conventional method is 11.84% whereas using the proposed method, the average discrepancy is reduced to 5.04%. Fig. 11(c) depicts the comparison at 300 V, where the average discrepancy in stator current prediction at varying loading levels reduced from 12.46% to 6.10% using the improved method.

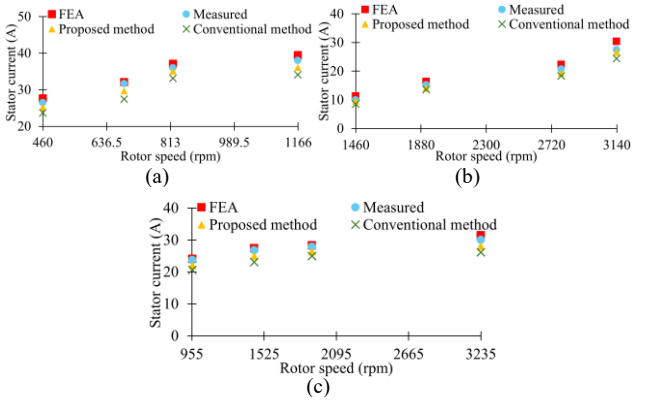

FIGURE 11. The behavior of traction IM's stator input current at varying rotor speed (rpm) under fixed voltage. (a) For voltage level 100 V under MTPA region. (b) For voltage level 200 V under MTPA and FW region (last data point). (c) For voltage level 300 V under MTPA and FW region (last data point).

C. MAGNETIZING INDUCTANCE WITH VARYING CURRENT UNDER A FIXED SPEED

The impact of the magnetizing inductance at varying stator input currents is investigated at a fixed speed. Fig. 12 (a), (b), and (c) presents the behavior of the magnetizing inductance at three different speed points. In this paper, magnetizing inductance is modelled considering the non–linearities using the non–variable power function, thus a comparison is drawn using the improved methodology. As depicted in Fig. 12, the comparison determines the improvement in the accuracy of the parameter such as magnetizing inductance prediction at different loading the MTPA region using the proposed methodology in the MTPA region improves the prediction accuracy by 5.49%, while using the conventional method's accuracy is compromised by 12.24% when compared with the experimental data. Furthermore, in the MTPA region shown in Fig. 12(b), the average discrepancy using the proposed method is reduced to 5.74% from 12.58% using the conventional method. Finally, Fig. 12(c) shows the FW region for increasing voltage. With respect to the experimental validation, the average discrepancy of magnetizing inductance prediction is reduced to 4.86% from 12.13~~3~~%.

D. MAGNETIZING INDUCTANCE WITH VARYING VOLTAGE UNDER A FIXED SPEED

This section investigates the profile of magnetizing inductance

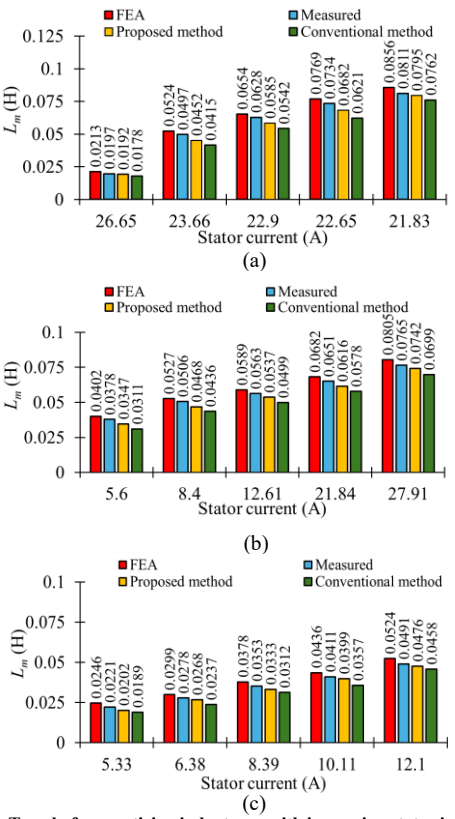

FIGURE 12. Trend of magnetizing inductance with increasing stator input current. (a) At 25 Hz under MTPA region. (b) At 66.67 Hz under MTPA region. (c) At 133.33 Hz under FW region.

at a fixed speed for varying voltage levels. With increasing voltage, the magnetic flux in the motor increases until reaching the saturation point. Beyond this point, the rate of change of flux with respect to voltage decreases, leading to a reduction in magnetizing inductance. Furthermore, higher voltage increases core losses such as eddy current and hysteresis core losses that contributes towards the reduction in the magnetizing inductance. As the MUT in this paper is an IM, a higher voltage drop is seen across the magnetizing inductance, leading towards a decrement in the inductance. Using the proposed methodology, an in–depth analysis of the MUT in terms of parameters prediction can be performed to determine the electromagnetic torque with higher accuracy. As presented in Fig. 13(a), at a fixed speed point in the MTPA region, the average discrepancy of magnetizing inductance prediction is improved by 5.74% with respect to the measured data.

However, the conventional method shows around 11.09% of the average discrepancy. Moreover, Fig. 13(b) shows the comparison at a fixed speed point in the MTPA region for the increasing voltage level. It can be seen that using the proposed method the average discrepancy is reduced from 12.58% to 5.87% in reference to the measured data.

Finally, Fig. 13(c) depicts the comparison of the magnetizing inductance at various voltages at a fixed speed point in the FW region. The average discrepancy in the magnetizing inductance parameter prediction reduced from

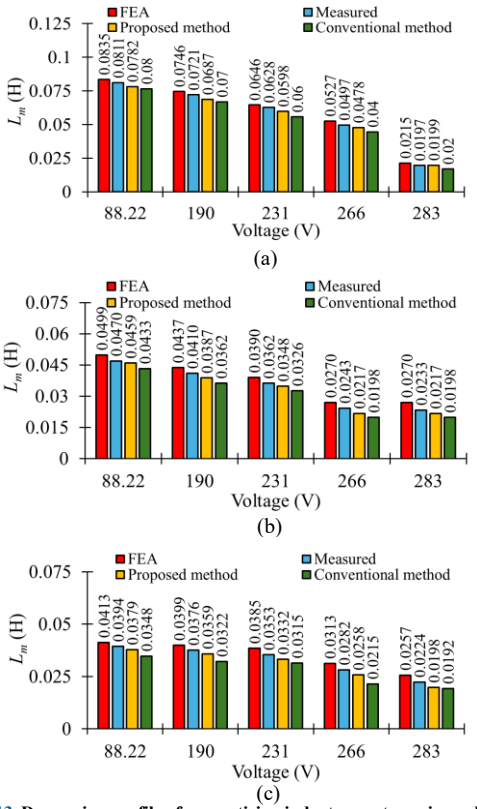

FIGURE 13. Decreasing profile of magnetizing inductance at varying voltage levels. (a) At 25 Hz under MTPA region. (b) At 66.67 Hz under MTPA region. (c) At 133.33 Hz under FW region.

15.20% to 6.34% using the improved method considering the experimental measurements as a reference.

E. IMPROVEMENT IN TORQUE PREDICTION AT VARYING FREQUENCIES

The modelling of inductances and resistance by incorporating the machine non–linearities is used to determine the electromagnetic torque accurately over a wide range of frequencies. A gear ratio is used to overcome the mechanical limitation during the testing therefore, in the MTPA region for a higher speed (≤ 3,000 rpm), the last two data points are not producing the maximum torque as shown in Fig. 14. Nevertheless, using the proposed method, a significant improvement in the prediction accuracy is observed in Fig. 14. The average discrepancy of electromagnetic torque prediction is improved by 5.50%, whereas, using the conventional method the torque predicted observed to be around 14.62%.

Therefore, modelling the electrical parameters such as magnetizing inductance, rotor leakage inductance, stator resistance and rotor resistance precisely by considering the non–linearities significantly improves the electromagnetic torque prediction at a wider range of frequencies.

V. CONCLUSION

The work carried out in this paper presents an improved modelling of IM inductances using power–function based formulation. The effect of MMF harmonics on the motor inductances is incorporated. Furthermore, the impact of temperature on magnetizing inductance using a proposed univariable power–function is investigated and considered. Additionally, for accurate prediction of rotor leakage inductance and rotor resistance, the permeance of rotor tooth–bridge segment is precisely formulated. For the validation of the prediction accuracy, 13 kW IM prototype is used. Using the proposed method, the prediction of the magnetizing inductance at various currents and voltages achieved high accuracy of 5.36%, and 5.98%, respectively. This is in comparison to the 12.31%, and 12.95%, accuracies attained with conventional method in the same order. Using the proposed method, the improvement in inductance modelling led to a 5.50% enhancement in the accuracy of electromagnetic torque prediction, reducing the average discrepancy from 14.62%, over a wide range of operating speed points.

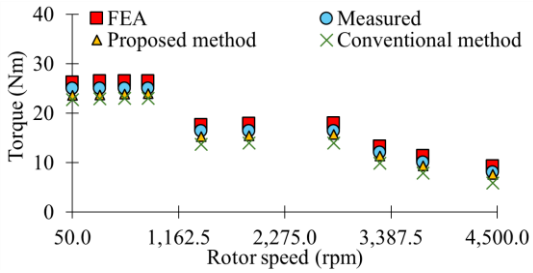

FIGURE 14. Electromagnetic torque prediction using the proposed methodology compared to experiments, FEA model, and conventional methodology.

Therefore, the proposed method can be applied to traction applications, facilitating in–depth performance analysis of traction motors over a wide range of operations.

ACKNOWLEDGMENT

Authors thank Canada Research Chair program (Ref.no. CRC−2019−00319), NSERC, Ford Motor Company of Canada, Nemak Engineering Centre for funding support to this work.

REFERENCES

[1] X. E. Yu, Y. Xue, S. Sirouspour, and A. Emadi, "Microgrid and transportation electrification: A review," in *Proc. IEEE Transp. Electrific. Conf. Expo*., USA, 2012, pp. 1–6.

[2] M. Popescu, J. Goss, D. A. Staton, D. Hawkins, Y. C. Chong, and A. Boglietti, "Electrical vehicles—Practical solutions for power traction motor systems," *IEEE Trans. Ind. Appl.*, vol. 54, no. 3, pp. 2751–2762, May/Jun. 2018.

[3] C. Liu, K. T. Chau, C. H. T. Lee, and Z. Song, "A critical review of advanced electric machines and control strategies for electric vehicles," in *Proc. IEEE*, vol. 109, no. 6, pp. 1004-1028, June 2021.

[4] D. Zechmair and K. Steidl, ''Why the induction motor could be the better choice for your electric vehicle program,'' *World Electr. Veh. J.*, vol. 5, no. 2, pp. 546–549, Jun. 2012.

[5] E. Mölsä, *et al*., "A dynamic model for saturated induction machines with closed rotor slots and deep bars," *IEEE Trans. Energy Conv.*, vol. 35, no. 1, pp. 157-165, March 2020.

[6] Zhang *et al*., "Optimization and experimental validation of amorphous alloy high-speed asynchronous motor for simultaneous reduction on core and copper losses," *IEEE Access*, vol. 11, pp. 101112-101122, 2023.

[7] M. Lavanya, P. Selvakumar, S. Vijayshankar, and C. Easwarlal, "Performance analysis of three phase induction motor using different magnetic slot wedges," in *Proc. 2nd Int. Conf. Elect. Energy Syst*., Chennai, India, 2014, pp. 164–167.

[8] Y. Xu, X. Bao, W. Xu, J. Fang, and T. Hong, "A method for improving power factor in inverter-fed induction motors by the use of rotor convex copper bars," *IEEE Trans. Ind. Appl.*, vol. 56, no. 4, pp. 3636-3643, July-Aug. 2020.

[9] A. Yahiaoui and F. Bouillault, "Saturation effect on the electromagnetic behaviour of an induction machine," *IEEE Trans. Magn.*, vol. 31, no. 3, pp. 2036–2039, May 1995.

[10] C. Gerada, K. J. Bradley, M. Sumner, and P. Sewell, "Evaluation and modelling of cross saturation due to leakage flux in vector controlled induction machines," *IEEE Trans. Ind. Appl*., vol. 43, no. 3, pp. 694–702, May/Jun. 2007.

[11] D. Gerada, A. Mebarki, N. L. Brown, K. J. Bradley, and C. Gerada, "Design aspects of high-speed high-power-density laminated rotor induction machines," *IEEE Trans. Ind. Electron*., vol. 58, no. 9, pp. 4039–4047, Sep. 2011.

[12] D. Gerada, A. Mebarki, N. L. Brown, K. J. Bradley, and C. Gerada, "Design aspects of high-speed high-power-density laminated-rotor induction machines," *IEEE Trans. Ind. Electron.*, vol. 58, no. 9, pp. 4039–4047, Sep. 2011.

[13] V. Fireteanu, T. Tudorache, and O. A. Turcanu, "Optimal design of rotor slot geometry of squirrel-cage type induction motors," in *Proc. IEEE Int. Electr. Mach. Drives Conf*., Antalya, Turkey, May 2007, pp. 537–542.

[14] J. H. Yun and S. B. Lee, "Simplified approach for predicting the starting performance of induction machines based on rotor design modification," *IEEE Trans. Magn*., vol. 53, no. 6, pp. 1-4, Jun. 2017, Art. no. 7206604.

[15] T. Gundogdu, Z. Q. Zhu, J. C. Mipo, and P. Farah, "Influence of magnetic saturation on rotor bar current waveform and performance in induction machines," *2016 XXII Int. Conf. Electr. Mach.,* (*ICEM*), Lausanne, Switzerland, 2016, pp. 391-397.

[16] A. C. Smith, R. C. Healey, and S. Williamson, "A transient induction motor model including saturation and deep bar effect," *IEEE Trans. Energy Conv*., vol. 11, no. 1, pp. 8–15, Mar. 1996.

[17] R. C. Healey, S.Williamson, and A. C. Smith, "Improved cage rotor models for vector controlled induction motors," *IEEE Trans. Ind. Appl*., vol. 31, no. 4, pp. 812–822, Jul./Aug. 1995.

[18] S. D. Sudhoff, D. C. Aliprantis, B. T. Kuhn, and P. L. Chapman, "An induction machine model for predicting inverter-machine interaction," *IEEE Trans. Energy Conv*., vol. 17, no. 2, pp. 203–210, Jun. 2002.

[19] S. D. Sudhoff, D. C. Aliprantis, B. T. Kuhn, and P. L. Chapman, "Experimental characterization procedure for use with an advanced induction machine model," *IEEE Trans. Energy Convers.*, vol. 18, no. 1, pp. 48–56, Mar. 2003.

[20] E. Mölsä, L. Tiitinen, S. E. Saarakkala, L. Peretti, and M. Hinkkanen, "Standstill identification of an induction motor model including deep-bar and saturation characteristics," *IEEE Trans. Ind. Appl.*, vol. 57, no. 5, pp. 4924-4932, Sept.-Oct. 2021.

[21] S. Williamson and M. C. Begg, "Calculation of the bar resistance and leakage reactance of cage rotors with closed slots," *IEE Proc. B Elec. Power Appl*., vol. 132, no. 3, pp. 125–132, May 1985.

[22] N. R. Klaes, "Parameter identification of an induction machine with regard to dependencies on saturation," *IEEE Trans. Ind. Appl*., vol. 29, no. 6, pp. 1135–1140, Nov./Dec. 1993.

[23] H. C. J. de Jong, "Saturation in electrical machines," in *Proc. ICEM*, Athens, Greece, Sep. 1980, vol. 3, pp. 1545–1552.

[24] T. Tuovinen, M. Hinkkanen, and J. Luomi, "Modeling of saturation due to main and leakage flux interaction in induction machines," *IEEE Trans. Ind. Appl.*, vol. 46, no. 3, pp. 937-945, May-June 2010.

[25] H. Chen, J. Zhang, J. Zhao, S. Qu, and Y. Zhou, "Analytical calculations of magnetic fields induced by MMF spatial harmonics in multiphase cage rotor induction motors," *IEEE Trans. Magn.*, vol. 57, no. 10, pp. 1-12, Oct. 2021.

[26] G. -Y. Zhou and J. -X. Shen, "Current harmonics in induction machine with closed-slot rotor," *IEEE Trans. Ind. Appl.*, vol. 53, no. 1, pp. 134-142, Jan.-Feb. 2017.

[27] S. Williamson and Y. N. Feng, "Slot-harmonic fields in closed-slot machines," *IEEE Trans. Ind. Appl*., vol. 44, no. 4, pp. 1165–1171, Jul./Aug. 2008.

[28] H. J. Lee, S. H. Im, D. Y. Um, and G. S. Park, "A design of rotor bar for improving starting torque by analyzing rotor resistance and reactance in squirrel cage induction motor," *IEEE Trans. Magn.*, vol. 54, no. 3, pp. 1-4, March 2018.

[29] J. Marault, A. Tounzi, F. Gillon, and M. Hecquet, "Efficient approach based on equivalent electric circuit model to determine rotor bar currents of squirrel cage induction machines," *IEEE Trans. Magn.*, vol. 57, no. 2, pp. 1-5, Feb. 2021.

[30] I. Boldea, and S. A. Nasar, *The Induction Machine Design Handbook*, 2nd ed. Boca raton, FL, USA: CRC Press, 2010.

[31] R. Kumar and P. Kumar, "Core Loss Estimation for an Inverter-Fed Induction Motor with More Accurate Realization of Material Non-Linearity and Impact of Hysteresis Minor Loops," *IEEE Trans. Energy Conv.*, vol. 37, no. 1, pp. 327-336, March 2022.

[32] K. Yamazaki and Y. Kato, "Iron loss analysis of interior permanent magnet synchronous motors by considering mechanical stress and deformation of stators and rotors," *IEEE Trans. Magn*., vol. 50, no. 2, pp. 909–912, Feb. 2014.

[33] "IEEE Standard Test Procedure for Polyphase Induction Motors and Generators," *IEEE Std 112-2017 (Revision of IEEE Std 112-2004)*, vol. no. pp.1-115, Feb. 2018.

Areej Fatima (Student Member, IEEE) received B.Sc. and M.Sc. degrees from COMSATS University, Islamabad, Abbottabad, Pakistan, in 2016 and 2019, in Electrical Computer Engineering and Electrical Engineering, respectively. She is currently a Ph.D. candidate at Center for Hybrid Automotive Research and Green Energy (CHARGE) Labs at the Department of Electrical and Computer Engineering of the University of Windsor, ON, Canada. Her research interests include the design, analysis, optimization, modeling, and testing of electric machines for electrified vehicle applications. She is an active reviewer for the IEEE Transactions on Transportation Electrification, IEEE Transactions on Magnetics, IEEE Transactions on Energy Conversion, and IEEE

Transactions on Industrial Electronics. In 2022, she earned recognition as a star reviewer for IEEE Transactions on Energy Conversion.

Rajendra Kumar (Member, IEEE) received a B.E. degree in electrical engineering from SBCET, University of Rajasthan, Jaipur, India, in 2007, the MTech. degree in nuclear engineering and technology from the Indian Institute of Technology Kanpur, Kanpur, India, in 2010, and the Ph.D. degree from the Department of Electronics and Electrical Engineering, Indian Institute of Technology Guwahati, Guwahati, India, in 2022. He was a Postdoctoral Fellow with the University of Windsor's Centre for Hybrid Automotive Research and Green Energy (CHARGE), Windsor, ON, Canada from 2022 to 2024. His recent research areas include analysis, design, and testing of electric machines.

Ze Li (Member, IEEE) received the B.Eng. and M.Eng. degrees in mechanical engineering from the Xi'an University of Architecture and Technology, Xi'an, China, in 2012 and 2015, respectively, and the Ph.D. degree in electrical engineering from the University of Windsor, Windsor, ON, Canada, in 2021. He was an R&D engineer in electrified powertrain systems with the Ford Motor Company, Canada. He is currently a BEV engineer and lead engineer in advanced battery pack engineering with Ford Motor Company, US. He is also a senior research associate with the University of Windsor's Centre for Hybrid Automotive Research and Green Energy (CHARGE Labs), Windsor, ON, Canada. His research interests include modeling and controlling electric power converters and electrical machines as well as electrified/hybrid powertrain and battery testing, NVH, and performance analysis.

Glenn Byczynski (Member, IEEE), R&D Manager Nemak USA/CAN, received his Ph.D. degree in Metallurgy and Materials Science from the University of Birmingham in the U.K. in 2002. He holds a Master of Applied Science in Materials Science (1997) and Bachelor of Applied Science in Mechanical Engineering (1994) both from the University of Windsor. During his 27 year career in metal casting he has held several R&D and Engineering positions within Nemak and Ford Motor Company including R&D Manager for the European Business Unit of Nemak based in Germany (2007-2009) and Engineering Manager at the Nemak Windsor Aluminum Plant (2005-2006).

He was Chairman of the Detroit-Windsor Chapter of the American Foundry Society (AFS) in 2006, and is currently President of the Foundry Education Foundation Canada, and holds posts of Adjunct Professor at Toronto Metropolitan University, University of Windsor and of Industry Professor at McMaster University. He is also a registered Professional Engineer in the Province of Ontario and is a Fellow of the Institute of Materials, Minerals and Mining. Dr. Byczynski has over 50 academic publications and 2 patents related to the casting of metals.

Narayan C. Kar (Senior Member, IEEE) received the B.S. degree from Bangladesh University of Engineering and Technology, Dhaka, Bangladesh, in 1992 and the M.S. and Ph.D. degrees from Kitami Institute of Technology, Hokkaido, Japan, in 1997 and 2000, respectively, both in electrical engineering. He is a Professor with the Electrical and Computer Engineering Department, University of Windsor, where he is also the Director of the Centre for Hybrid Automotive Research and Green Energy (CHARGE). His research presently focuses on the analysis, design, and control of electrical machines for electrified vehicle applications; testing and performance analysis of batteries; and optimization techniques for hybrid energy management system.